Spatiotemporal Variability Relationships of Shallow Cloud Height and Planetary Boundary Layer Height Over the Northeast Pacific Using Satellite Observations and Reanalysis

To be Submitted to: *Journal of Geophysical Research - Atmospheres*

Terence L. Kubar[1,2]

Chi O. Ao[2]

Kuo-Nung Wang[2]

Jonathan H. Jiang[2]

[1]Joint Institute for Regional Earth System Science & Engineering, University of California, Los Angeles

[2]Jet Propulsion Laboratory, California Institute of Technology, Pasadena, California

---

Key Points:

- Northeast Pacific low cloud and PBL heights agree best when excluding profiles with low temperatures above the PBL or rising motion aloft.
- Cloud and PBL heights are enhanced (suppressed) when Oceanic Niño Index or Pacific Decadal Oscillation is positive (negative).
- Temperature anomalies above PBL top may provide forecasting skill up to 1.5 years of marine layer depth and low-topped cloud heights.

Abstract:

Over 18 years of satellite data from Multi-Angle Imaging Spectroradiometer (MISR) and 14 years from Global Navigation Satellite System-radio occultation (GNSS-RO), with ERA5 reanalysis temperature profiles, are used to assess the co-variability of cloud and thermodynamic properties of the Northeast Pacific subtropical marine boundary layer. Low cloud top height (CTH) inferred from MISR and planetary boundary layer height (PBLH) inferred from GNSS-RO are well-correlated spatially for all seasons when seasonally-varying mid-latitude grids (temperature at 700 hPa < 4°C) are removed (r=0.83), or when vertical velocity at 500 hPa (ω_{500}) indicates descent (r=0.74). The temporal correlation of PBLH and CTH is highest in the stratocumulus region (r=0.72), with the CTH versus PBLH slope close to one for heights between 0.8 km and 1.6 km of the time series. Seasonal sea-surface to 700 hPa lapse rate (LR) is spatially related with PBLH and more strongly with CTH, and ω_{500} modulates seasonal CTH-LR relationships. The impact of El-Niño Southern Oscillation (ENSO) through teleconnections on the PBL structure is also characterized, with maximum deseasonalized temperature anomalies near or above PBL top (near the surface) during La Niña (El Niño), with CTH, PBLH, and LR anomalies largest during the strong 2015-2016 El Niño. Temperature anomalies above the PBL lead CTH' and PBLH' by 15 and 18 months, respectively, just under half the time scale of the periodicity of an Ocean Niño Index mode (~3.1 years), suggestive of the role of atmosphere-to-ocean exchange manifesting in a deepening PBL during warm ENSO.

Plain Language Summary:

Two independent space-borne observational data sets characterize how well marine layer top heights correspond with low-level cloud heights over the Northeast Pacific Ocean region. Low cloud heights correlate best with marine layer heights seasonally and spatially when areas

exhibiting mid-latitude behavior of lower temperatures above marine layer top, and hence reduced stability based on reanalysis data, are excluded. Rising motion aloft decreases the capping strength of the marine inversion, less likely constraining clouds to the boundary layer. On interannual time scales, El-Niño Southern Oscillation and the Pacific Decadal Oscillation remotely influence the low-level temperature stability of the Northeast Pacific Ocean, with greater lapse rates, marine layer heights, and low cloud heights during periods of El Niño versus La Niña. During El Niño, temperature anomalies are greatest near the surface, destabilizing the lower atmosphere, with the highest anomalous ocean temperature greatest in spatial scale during the 2015-2016 event, and during La Niña, temperature anomalies are greater near or just above marine layer top, stabilizing and suppressing the marine layer depth and low cloud heights. Temperature anomalies above the marine layer may provide forecasting skill up to 1.5 years of the depth of low clouds and the marine layer.

1 Introduction

The planetary boundary layer (PBL) and low-level clouds are of profound importance both to the climate system and also to the regulation of near-surface air with the free troposphere. Closely related to how well-mixed the PBL is, the PBL height, through its tie to low-level stability, helps determine the concentration of near-surface pollution; deeper PBLs are inversely correlated with near-surface concentrations such as tropospheric ozone (O_3) and O_3 precursors (Dey et al., 2018). Over the oceanic tropics, the PBL height is also inversely related to precipitation owing to the relationship of stronger sensible heat fluxes during the dry season; during wet periods stronger latent heat fluxes move mass above the shallower PBL (Chan and Wood, 2013). In primary low cloud regions, PBL depth also helps control cloud type and coverage (Chan and Wood, 2013; Wood, 2012).

Marine oceanic low-level clouds have a net cooling effect on the climate system, owing to their high reflectivity compared to the ocean surface and only modestly cooler cloud top temperatures (e.g. Boucher et al., 2013; Hartmann et al., 1992; Randall et al., 1984), such that the shortwave cooling effect exceeds the modest longwave warming effect, but how low clouds may change in response to local or remote forcing on a variety of time scales may be critical for helping to constrain climate sensitivity estimates. As clouds and/or the PBL deepen in association with increases in sea-surface temperature (SST), a reduction in the lower tropospheric temperature in the upper boundary layer or near PBL top, or some combination thereof, low cloud breakup may ensue in conjunction with a weakened inversion and increased decoupling and entrainment by cumulus clouds in vigorous updrafts of dry free tropospheric air (e.g. Wyant and Bretherton 1997), making low cloud top height (CTH) and planetary boundary

layer height (PBLH) important markers of horizontal cloud cover and the amount of sunlight reaching the ocean surface.

Close to the coast, well-mixed clouds are generally shallowest and topped by stratus or stratocumulus (Sc) clouds, especially during summer when low-level stability is strongest. This is also where CTH and PBLH agree most closely with each other, at least over the Southeast Pacific (Kubar et al. 2020); however, mean CTH is often below PBLH in trade cumulus regions since not all clouds reach the trade inversion (Karlsson et al. 2010). This may also be the case for stratocumulus with underlying cumulus clouds, in which both a weak stable layer exists below the primary inversion base as well as a moist surface layer induced by relatively stronger upward latent heat fluxes. The cumulus clouds detrain into the stratocumulus clouds, and in broken Sc areas, the retrieved cumulus cloud top height is lower than the inversion layer (Zhou et al., 2015). As summarized in Zhou et al. (2015) of the Bretherton and Wyant (1997) study, the transition layer is below the radiatively-driven inversion height and above the surface layer of enhanced specific humidity; the upper part of the PBL thus is decoupled from the lower part (Jones et al., 2011). In such a PBL, the lapse rate from the surface to the lifting condensation level (LCL) is the dry abiabatic lapse rate (DALR), and the decoupled layer, between the surface mixed layer top and PBL inversion height, generally follows a moist adiabat (Wood and Bretherton, 2006).

The variability of low cloud fraction has often focused on the annual cycle (e.g. Klein and Hartmann, 1993; Kubar et al., 2012), though De Szoeke et al. (2016) have demonstrated the importance of the time scale between synoptic and seasonal. Recent work has examined changes in cloud-controlling factors to describe commensurate changes in low cloud fraction; using two decades of Terra and Aqua Moderate Resolution Imaging Spectroradiometer (MODIS)

data, Andersen et al. (2022) characterize a reduction in low cloud cover over the Northeast Pacific most concentrated between 13°N-23°N and 140°W-112°W. Corresponding large-scale environmental trends include an increase in SST and decreases in wind speed, subsidence strength, and estimated inversion strength (EIS), and a weak increase in free-troposphere relative humidity. The authors attribute natural variability to the trends. Incidentally, there's a nearly equal and opposite (positive) trend of low cloud cover in the SE Pacific (Andersen et al., 2022). Such north/south asymmetric trends are an amplification of already observed natural distribution of more low clouds over the southeast versus the NE Pacific.

Building on Kubar et al. (2020), hereafter KU20, the goal of this study is to characterize the spatiotemporal variability of CTH and PBLH, focusing on where there is consistency between PBLH and CTH, with results broken down seasonally, and also across the NE Pacific instead of the SE Pacific. While we expect agreement to be best over the shallowest to moderate-depth PBLs, such as stratus, stratocumulus, and the transition to trade cumulus regions, we aim to quantify CTH-PBLH relationships through statistical analysis. We also examine interrelated variables such as the lower tropospheric lapse rate and ω_{500}. Recently, Kalmus et al. (2022) have provided a global analysis of PBLH at the highest horizontal resolution publicly available to date from GNSS-RO, with the annual and diurnal cycle climatologies assessed. Our study is both more regional and addresses PBLH spatiotemporal relationships with satellite CTH measurements from Multi-Angle Spectroradiometer (MISR), in addition to low cloud/PBL-controlling variables of each. Temporally, we examine modes ranging from subannual to annual to interannual. For interannual variability, teleconnections such as El Niño Southern Oscillation (ENSO) and the Pacific Decadal Oscillation (PDO) may be important; during warm (cold) ENSO, SSTs are not only anomalously warm (cold) over the central and eastern equatorial

Pacific, but positive (negative) SST anomalies also extend poleward over the mid-and-high latitudes of the NE Pacific. The anomalous mid-latitude SST spatial patterns associated with both phases of ENSO are similar to those with the PDO, though PDO intrinsically encapsulates lower-frequency variability. We will quantify the role of these SST anomalies and co-located atmospheric temperature anomalies in driving the low-level lapse rate and hence PBLH and CTH anomalies.

2 Data

a. Multi-Angle Imaging Spectroradiomer (MISR)

For each gridded low CTH, we use over 18 years (April 2002 – August 2020) of monthly Level-3 MISR data from the cloud fraction by altitude (CFbA) product at 0.5°x0.5° horizontal resolution with 41 vertical levels and 500 m vertical sampling. The CFbA joint product, originally constructed from the L2 1.1 km nadir cloud fraction, represents the highest-resolution CFbA product of any passive instrument (Kubar et al., 2019; Di Girolamo et al., 2010). Compared to other passive satellites, MISR is particularly adept at measuring geometric cloud height directly without the need for external auxiliary profile data, since MISR is equipped with cameras in nine directions, one at nadir, four in the forward along-track, and four in the aft directions of nadir. We compare MISR CTH data both spatially and temporally to PBLH and lower tropospheric measures of thermodynamic stability. For a more detailed discussion of the technical qualities and specifications of MISR, please see Kubar et al. (2019).

The definition of low CTH is the mean height of all clouds in a 0.5°x0.5° grid between the ocean surface and 6 km, with weighting by the histogram of CF(z). For direct point-by-point comparisons, we linearly interpolate the higher resolution CTH grids onto the coarser GNSS-RO 2°x2° PBLH grids. This CTH vertical range includes possible clouds that are above the mean

177 PBL, which was also noted in de Szoeke et al. (2016); we employ seasonal temperature and
178 dynamic filters to separate out probable mid-latitude clouds.

179 *b. GNSS-RO*

180 Refractivity profiles retrieved from GNSS-RO measurements, which have high vertical
181 resolution (~200 m) and ~100-km horizontal resolution, contain temperature and moisture
182 information used to deduce PBL top in all-weather conditions (Anthes et al., 2008; Kursinski et
183 al., 2000). Specifically, PBLH is determined from each profile by locating the height of the
184 minimum refractivity gradient below 6 km (Ao et al., 2012; Basha and Ratnam, 2009; Xie et al.,
185 2012). At low to middle latitudes, a large refractivity gradient is largely dictated by the moisture
186 and temperature gradient across the PBL top (Ao et al. 2012; Chan and Wood, 2013). Here, we
187 use monthly-averaged 2°x2° PBLH derived from the JPL v2.6 Level 2 refractivity products from
188 the COSMIC, TerraSAR-X, KOMPSAT-5, and PAZ GNSS-RO missions spanning the period of
189 Jun. 2006– Dec. 2020 (Kalmus et al. 2022).

190 *c. ERA5 Reanalysis*

191 We use monthly SST, low-level temperature profile information, and ω_{500} gridded at
192 0.25°x0.25° from the European Center for Medium Range Forecasts Version 5 (ERA5) to
193 calculate lower tropospheric lapse rates (LR) (Hersbach et al., 2020). With a decade of
194 development since ERA-Interim, ERA5 has the advantage of updated model physics, core
195 dynamics, and data assimilation, with over twice the horizontal resolution. Note that we use
196 ERA5 SST data for the NE Pacific area, with the teleconnection data selection described below.

197 *d. ENSO and PDO*

198 The Oceanic Niño Index (ONI), one of several ENSO indices, is calculated by the three-
199 month running mean of SST anomalies in the Niño-3.4 region between 170°W-120°W and 5°S-

5°N, with the anomalies computed with respect to 30-year base periods updated every five years, and 2°x2° monthly SSTs from the Extended Reconstructed SSTs (ERSST) version 5 (Huang et al., 2017). ONI is used directly from the from the Climate Prediction Center ENSO data, acquired from https://origin.cpc.ncep.noaa.gov/products/analysis_monitoring/ensostuff/ONI_v5.php. The Pacific Decadal Oscillation (PDO) is frequently characterized by a long-duration ENSO-like pattern of North Pacific climate variability (Zhang et al., 1997; Mantua and Hare, 2002), with some overlapping teleconnection patterns over both the Pacific Ocean and North America with ENSO. The PDO index represents the first mode of the EOF of the SST anomalies of the North Pacific (poleward of 20°N), after removal of the global mean SST, referred to as "residuals" in Mantua and Hare (2002). A positive/warm PDO phase (as represented by the first principle component amplitude) occurs when the western/interior north Pacific is anomalously cool with anomalous high pressure and the eastern north Pacific is anomalously warm, while during a cool, or negative phase, the western/interior Pacific is anomalously warm and the eastern North Pacific is anomalously cool. PDO data for this study were acquired from https://www.ncei.noaa.gov/pub/data/cmb/ersst/v5/index/ersst.v5.pdo.dat, which like the ONI time series, are constructed from the ERSST anomalies; the NCEI PDO index used here similarly adheres to the Mantua PDO index.

3. Spatial Analysis Results

The first part of this paper focuses on the horizontal distribution of PBLH, CTH, and LR as a function of season, including the degree of agreement between PBLH and CTH as well as the goodness of fit between PBLH/CTH and LR, and we also examine the separate roles of temperature at 700 hPa (T_{700}) and ω_{500}.

223 The maximum PBLH over the region, regardless of season, occurs over the southwestern
224 portion of the domain (Figure 1a, 1d, 1g, and 1j), and the shallowest PBLs are found generally in
225 the east, and more specifically the northeast portion. The shallowest clouds are also found in the
226 eastern portion, with a shift of the shallowest heights north during summer (Figure 1h) and
227 further south during winter and spring (Figure 1b, 1e). The coherence between PBLH and CTH
228 is especially high in the eastern part of the NE Pacific. However, while CTH is broadly higher in
229 the west, maximum CTH is observed in the northwestern part of the domain, with the highest
230 low clouds during DJF, whereas the deepest PBLs occur during SON. The LR distribution
231 generally follows a similar spatial pattern with season as CTH, with a clear maximum in the
232 western/northwestern part of the domain during DJF. Minimum lapse rates are observed during
233 summer, especially along the west coast of the U.S. extending to the west coast of Baja
234 California.

235 In Figure 1m, we present the annual cycle of PBLH and CTH., Both datasets agree that PBLH
236 and CTH are shallowest during summer, though PBLH maximizes during SON, and CTH during
237 DJF. The amplitude of the annual cycle (maximum minus minimum) is 0.24 km for PBLH and
238 0.38 km for CTH. We note that estimates of PBLH from reanalysis also suggest maximum
239 seasonal heights during SON (not shown).

240 The annual cycle of LR (Figure 1n), like CTH, maximizes during DJF, minimizes during JJA,
241 and is second largest during SON. The two components of LR, SST and temperature at 700 hPa
242 (T_{700}), are also presented, with SST lagging T_{700} by a season, e.g. free-tropospheric temperatures
243 maximize during JJA, but SSTs continue to warm from JJA to SON, which is likely due to the
244 large thermal inertia of the ocean. Similarly, T_{700} is lowest during winter (DJF), but SST bottoms
245 out one season later (spring, MAM). The amplitude of SST is smaller than the amplitude of

246 T_{700}, of 3.14°C versus 4.98°C, respectively, and the peak-to-peak amplitude of the regional LR is
247 about 1.0°C km^{-1}.

248 In the left panels of Figure 2, we present seasonal scatterplots of CTH versus PBLH, and
249 include seasonal slopes using the least absolute deviation method (LADFIT), Pearson linear
250 correlation coefficient (r), and the root-mean square error (RMSE). As we may have anticipated
251 from the

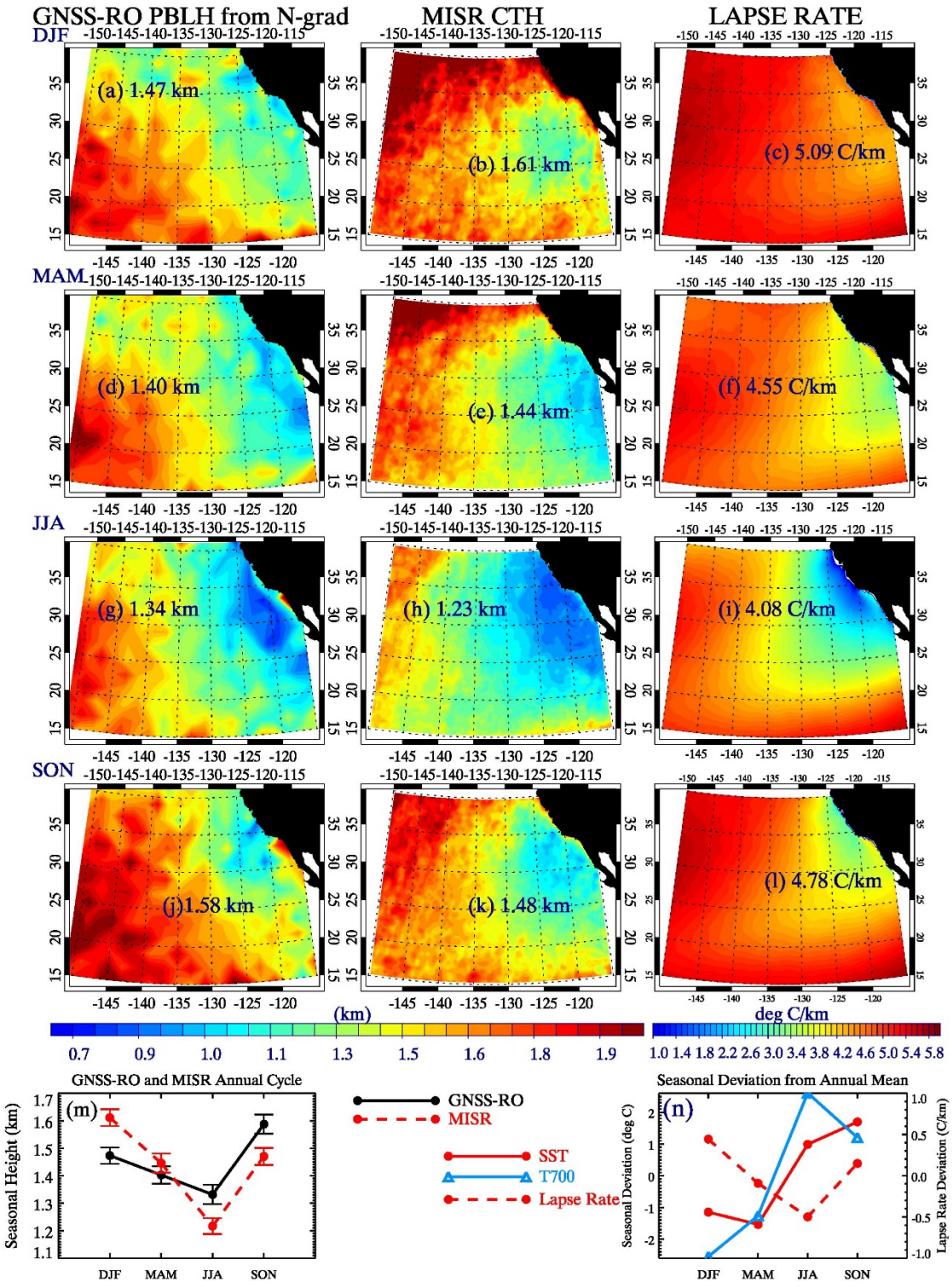

Figure 1. (a), (d), (g), and (j): Seasonally-averaged PBL heights for DJF, MAM, JJA, and SON in km. (b), (e), (h) and (k): Same as (a), (d), (g), and (j), except CTH (c), (f), (i) and (l): Same as (b), (e), (h), and (k) except for LR (°C/km). (m) Annual cycle of PBLH and CTH. (n) Seasonal annual deviation for SST, temperature at 700 hPa, and LR.

seasonal maps in Figure 1, CTH is imperfectly correlated with PBLH, with the least correlation (r=0.30) and largest RMSE (0.297 km) during DJF, and the best fit and smallest RMSE during summer (r=0.83 and RMSE=0.185 km). CTH-PBLH slopes are always below one, meaning that CTH increases more slowly for a given increase in PBLH, though slopes are more similar during MAM, JJA, and SON (0.73, 0.67, and 0.63, respectively) and the slope is greatly reduced during DJF (0.35).

Especially during DJF and MAM, there is a sizeable subset of low cloud tops which substantially exceed PBLH. We highlight where these are spatially with contour maps in the middle column of Figure 2 of PBLH minus CTH; PBLH << CTH primarily in the northern part of the domain during DJF and MAM, which is under the influence of mid-latitude clouds and the seasonal storm track. The greater equatorward shift of baroclinic instability during winter versus summer was shown in Behrangi and Kubar (2012), and also tracks quite well with temperature at 700 hPa (T_{700}), superimposed as unfilled contours in increments of 2°C. In accord with reduced baroclinicity during JJA and SON, there are relatively few clouds above the PBL top during those seasons. During DJF, 24% of CTH observations are greater than 0.3 km larger than PBLH, and 11% are during MAM, and only 1% of grids are during either JJA or SON.

The observation that the slope is less than one for all seasons means that particularly for deeper PBLHs, not all cloud tops reach PBL top. In KU20, MODIS also suggested this relationship in the SE Pacific versus GNSS-RO PBLH (KU20), with daily MODIS CTH leveling off around 2 km for PBLH>2km.

Larger CTH minus PBLH differences are observed when baroclinicity is higher since our method for computing CTH for each grid for each month is weighted by cloud fraction as a

function of height for all clouds with tops between 0-6 km. As such, there can be multiple observed

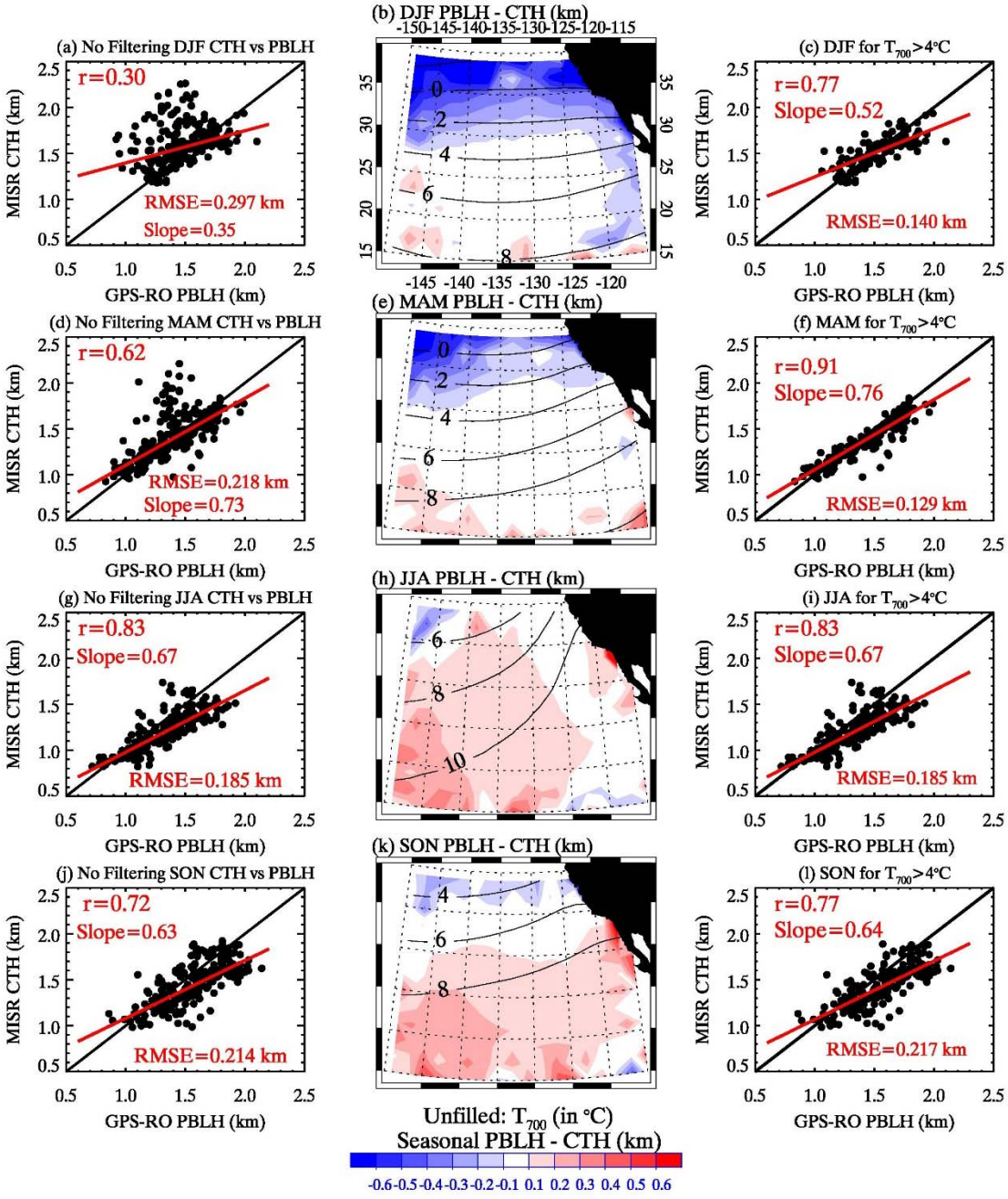

Figure 2. Seasonal scatterplots of CTH versus PBLH for (a) DJF, (d) MAM, (g) JJA, and (j) SON. Middle column: Seasonal PBLH minus CTH (in km) for (b) DJF, (e) MAM, (h) JJA, and (k) SON, depicted by filled contours. White areas indicate differences between -0.1 km and +0.1 km. Unfilled contours denote seasonal 700 hPa temperatures in increments of 2°C. (c), (f), (i), and (l): Same as (a), (d), (g), and (j), except only for seasonal grids with T_{700}>4°C. In the left column and right column, the one-to-one line (black) and the least absolute deviation linear fit (red line) are shown. Also shown in the left and right

columns are the r-value, slope, and the root-mean square error in km. For seasonal grids in which T_{700}>4°C, mean (PBLH-CTH)=14-m for DJF, 60-m for MAM, 115-m for JJA, and 138-m for SON.

cloud tops in a 0.5°x0.5° grid. In contrast, in trade cumulus areas, PBLH > CTH in the southwestern parts of the domain, exceeding 200 m especially where T_{700}>8°C. There is also a small area in which PBLH>CTH near the extreme southern California Coast and Baja California during JJA and SON; this also is an area of strong local SST and LR gradients, with potential effects of GNSS-RO averaging partial land grids.

The right column of Figure 2 shows CTH vs PBLH seasonal scatterplots filtered only for seasonal grids in which T_{700}>4°C, thus preferentially selecting seasonal subtropical grids. CTH-PBLH relationships are most impacted by this filtering during DJF and MAM, which greatly improves the correlation and reduces the scatter; RMSE is only 0.140 km and 0.129 km for DJF and MAM, respectively, and r=0.77 and r=0.91, respectively, much higher than r=0.30 and r=0.62 when the whole domain is considered. The slope for DJF for only grids in which T_{700}>4°C is more similar although still slightly reduced to the other seasons. This suggests that a colder free troposphere is associated with a higher lapse rate and large-scale dynamics connected to mid-level clouds that diminishes the one-to-one agreement between PBLH and CTH for all PBLs/CTHs between 0-6 km.

Next, we wish to understand if related large-scale factors might further explain the presence of cloud tops above PBLH, especially during DJF and MAM, and since our definition of low clouds is generous, we examine the potential impact of ω_{500}, with 500 hPa generally between 5-6 km depending on location. Weaker subsidence, or even weak to modest ascent, may contribute to clouds above the PBL. Figure 3a presents seasonal ω_{500} versus LR scatterplots, with all seasons included in one panel to highlight differences. We invert the y-axis from positive to negative so that going up means weaker subsidence, or for positive ω_{500}, ascending motion. Relationships of

ω_{500} versus LR during JJA (red filled circles) and SON (orange crosses) are more similar to each other; especially during JJA ω_{500} is nearly invariant with increasing LR for 1°C/km < CTH < 4°C/km, with then a stronger reduction in subsidence strength for larger LR; summer is also the only season for mean LR<3°C/km grids are observed. The -ω_{500}-LR slope for SON is slightly stronger, and both MAM and DJF have much larger -ω_{500}-LR slopes.

Seasonal CTH strongly increases with LR for a given season or in the aggregate (Figure 3b), and we show the least-squares exponential fit, with an r-value of 0.88, which is slightly more skillful than a linear fit (r=0.85). Two distinguishing features for DJF and MAM are sharp increases of CTH for a subset of the NE Pacific above the predicted fit for LR just under 5°C/km for MAM and around 5.5°C/km for DJF; this is similar behavior as ω_{500}, with corresponding ascending motion with these LR. The qualitative similarity between panel (a) and panel (b) suggests that free-tropospheric vertical velocity may be modulating CTH-LR behavior.

Seasonal PBLH vs LR has more scatter than CTH vs LR, but similar to CTH, a least-squares exponential fit (r=0.73) is slightly more skillful than a linear fit (r=0.71). One of the main differences, as we may have expected form Figure 1, is that during SON, PBLH tends to be above the predicted values from the least-squares exponential fit; this offset cannot be readily explained by either seasonal LR or ω_{500} differences versus other seasons.

We also compare the behavior of both CTH and PBLH versus ω_{500} (Figure 3d), and see that there is considerable overlap with increasing CTH or PBLH with decreasing free-tropospheric subsidence strength in subsidence regimes, but for ascending motion grids, PBLH is nearly invariant with decreasing ω_{500}, whereas CTH appears to exhibit more of a monotonic increase with decreasing subsidence and increasing ascent.

To make these points even more obvious, in Figure 3f we plot CTH vs PBLH for grids with descent (ω_{500} > 5 mb/day; black dots) and those with near-neutral conditions or ascent (ω_{500} < 5

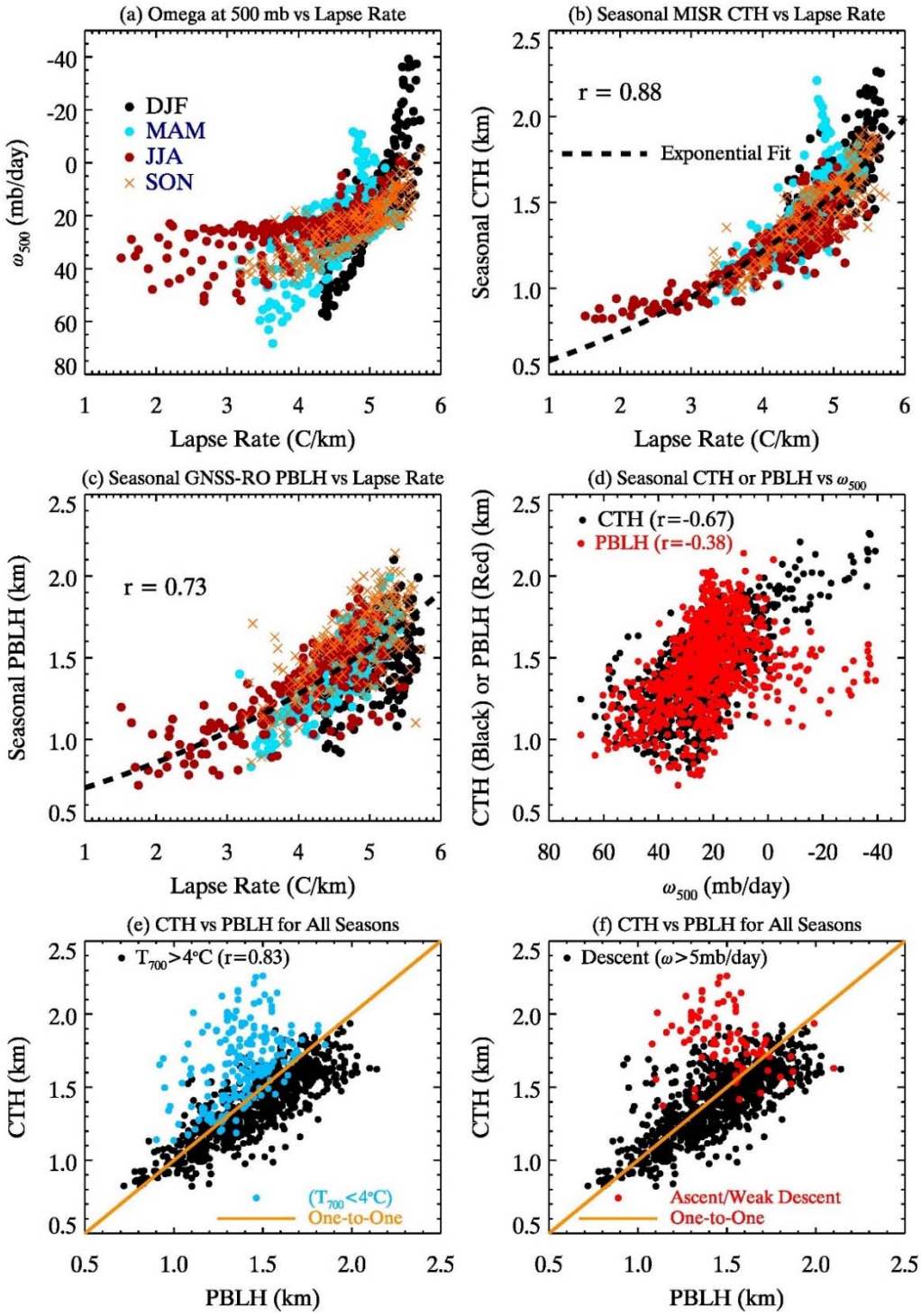

Figure 3. (a) – (c) Seasonal scatterplots versus LR of (a) ω_{500}, (b) CTH, and (c) PBLH, with black dots denoting DJF, light blue dots denoting MAM, red dots denoting JJA, and orange crosses denoting SON.

Best exponential fit lines and r-values given in (b) and (c). (d) Seasonal CTH vs ω_{500} (black dots) and PBLH vs ω_{500} (red dots), with r-values given in legend. (e) CTH vs PBLH for all seasons in which T_{700}>4°C (black dots) and T_{700}<4°C. (f) CTH vs PBLH for descending grids (ω_{500}>5 mb/day; black dots) and weak seasonally-descending/ascending grids (ω_{500}<5 mb/day; red dots). For all grids, r(PBLH,CTH)=0.62, and for ω_{500}>5 mb/day, r(PBLH,CTH)=0.74.

mb/day; red dots), with generally good agreement for descending grids, and CTH usually much larger than PBLH for near-neutral or ascending seasonal grids. When all seasonal grids are included, r(PBLH,CTH)=0.62, but for descending grids with ω_{500}>5 mb/day, r=0.74. Thus, excluding free-tropospheric ascent improves the consistency between the two sets of observations. For a nearly analogous comparison, but with T_{700} as a filter, in Figure 3e we show CTH vs PBLH for our previous constraint of T_{700}>4°C (black) and T_{700}<4°C (blue); for T_{700}>4°C the r-value of all seasons is 0.83, suggesting greater improvement in agreement between CTH and PBLH with a thermodynamic rather than dynamic (ω_{500}>5 mb/day) constraint, though both constraints remove outliers from a presumed linear fit.

4 Temporal and Spatiotemporal Analysis

We next examine time series across the entire NE Pacific domain as well as subregions defined by their percentiles. Percentiles of variables naturally move spatially, offering a measure of distribution changes over time.

We begin with the time series of the 25th and 75th percentiles of monthly PBLH and CTH (Figure 4a), starting in 2006 for PBLH and 2002 for CTH. The 25th percentiles of PBLH and CTH closely track each other in time, with a temporal correlation of r=0.72 (Figure 4e), whereas the 75th percentiles are often out-of-phase by up to a few months; CTH_{75th} peaks near the beginning of each year and $PBLH_{75th}$ peaks during SON. Based on our earlier seasonal spatial analysis, the location of deepest PBLHs (southwestern part of the domain) is not in the same place as the deepest low clouds (northern/northwestern part of the domain). The standard deviation, a good proxy of the annual cycle amplitude, is greater for CTH_{75th} (0.22 km) than for

$PBLH_{75th}$ (0.16 km). Standard deviations of PBLH and CTH are very similar especially for the bottom 50% of the distribution for each variable, above which σ_{CTH} begins to exceed σ_{PBLH} (Figure 4d). The lapse rate standard

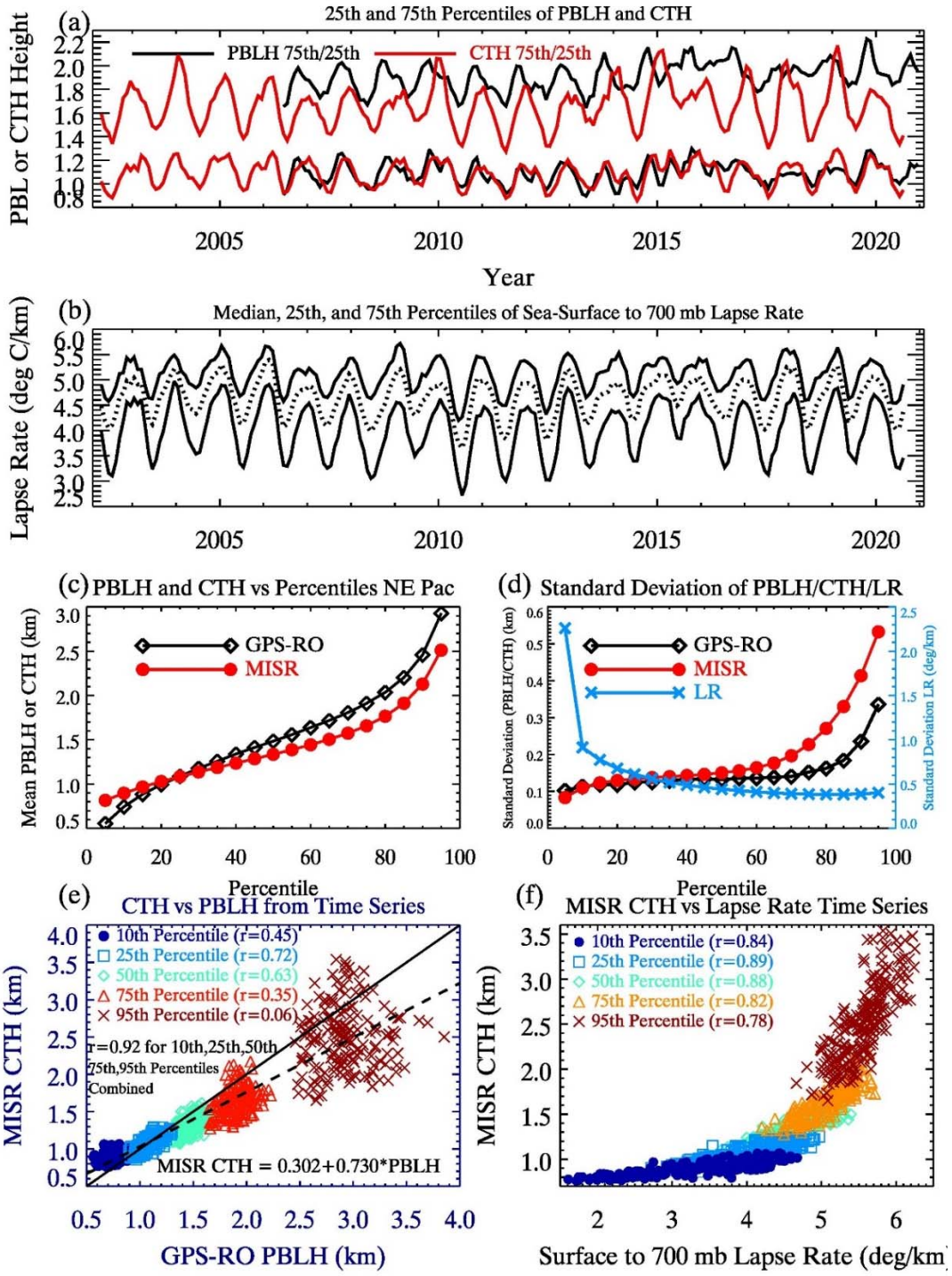

Figure 4. (a) Time series of domain-averaged PBLH and CTH 25th and 75th percentiles. (b) Same as (a), except for LR and also including the median time series. (c) Mean PBLH and CTH vs percentile (d) Standard deviation of PBLH, CTH, and LR versus percentile. (e) CTH versus PBLH for selected percentiles. (f) Same as (e), except for CTH versus LR. In (e), one-to-one and least absolute deviation linear fit lines are shown.

deviation *decreases* with percentile, which is apparent either from Figure 4b or the blue curve in Figure 4d. When we examine the CTH percentiles versus LR percentiles (Figure 4f), any given CTH percentile is fairly well correlated within any LR percentile, with the highest r-values for the 25th-50th percentiles, but the shape of CTH percentiles among different LR percentiles appears to be *exponential* due to the reverse behavior of the standard deviation behavior of each.

We next shift to time series of anomalies, calculated by removing the annual cycle, using a reference climatology at each grid or subregion for each month. We present time-longitude Hovmöller diagrams latitudinally-averaged between 15°N-40°N. The focus is on interannual variability, with the possible identification of west-east propagation of features of anomalies on shorter time scales. First, we regrid ERA5 variables to MISR CTH' resolution, and perform a boxcar average of width three in each direction for all variables, meaning 3-month smoothing in time and 1.5° smoothing in longitude.

The Hovmöllers in Figure 5 include (a) CTH', (b) LR', (c) SST', and in panel (d), ONI is presented with red dots denoting months of El Niño (ONI>0.5°C), black dots denoting neutral conditions (-0.5°C<ONI<0.5°C), and blue dots denoting La Niña (ONI<-0.5°C). Due to the greater sparsity, we are not able to present PBLH Hovmöller diagrams. Particularly for CTH' and LR', periods of positive anomalies tend to coincide temporally with El Niño periods, and periods of negative anomalies coincide temporally with La Niñas. We draw red and blue boxes during periods of more sustained (temporally) positive and negative anomalies for CTH', LR', and SST'.

The strongest El Niño of the record peaks in late 2015/early 2016 (Figure 5d), which coincides with a period of enhanced CTH', LR', prolonged high SST', and even warm T700' (not shown). There appears to be propagating west-to-east positive CTH' and LR' from early 2015 in the west to the eastern boundary in late 2015/2016, but there is also localized east-to-west movement

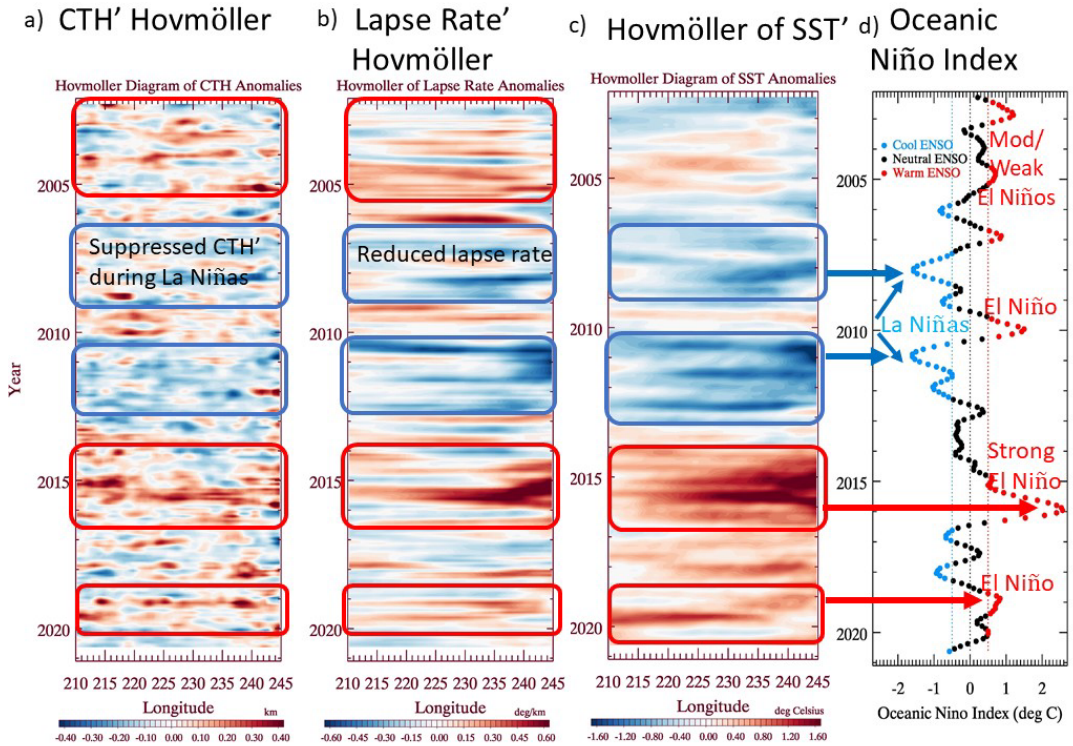

Figure 5. Hovmöller diagrams across the NE Pacific domain (15°N-40°N) for (a) CTH', (b) LR', (c) SST', and d) ONI. Red (blue) boxes in (a), (b), and (c) designate when anomalies tend to be positive (negative), corresponding with periods of more active El Niños (La Niñas). In (d), thin red dashed line represents threshold above which El Niños exist (ONI>0.5°C), and thin blue dashed line below which La Niñas (ONI<-0.5°C) exist. Anomalies are calculated by removing the annual cycle from the reference period for each dataset.

especially of LR' and SST' from the coast in early 2015 westward later in the year. High SST anomalies may also be connected to the broader marine heat wave over the northeast Pacific from 2013-2015 (Myers et al. 2018). Consistent with a Terra-MODIS analysis of low cloud

fraction by Myers et al. (2018), MISR indicates suppressed low cloud fraction starting in 2014, with the least amount of low cloud in much of 2015 (not shown).

Spatiotemporally, SST' and T700' are weakly correlated (r=0.38), and 14% of the variance of SST' can be explained by T700'. SST' is more spatiotemporally correlated with LR', with r=0.63 (r^2=0.40), but without temporal smoothing, T700' is more strongly anticorrelated with LR' (r = -0.71). This suggests a smaller intrinsic temporal autocorrelation of free-tropospheric temperature compared to the ocean surface. In contrast, T700' is only weakly anticorrelated with CTH' (r=-0.25) (no smoothing), whereas CTH' and SST' are modestly more correlated (r=0.37) using a boxcar average of width 3x3, and r=0.48 for LR' and CTH' for the same smoothing.

West-to-east propagation of LR' and SST' precedes some La Niñas; in mid-2010 a negative LR anomaly travels from west-to-east across the domain, leading to sustained negative LR' for more than a year in the east; similar propagation of SST occurs in concurrence. When ONI denotes La Niña from late 2010 through early 2012, a double-dip La Niña, there are three instances of negative pulses of negative LR' and SST', some apparently propagating in a west-to-east manner and some occurring simultaneously across the domain. Despite more noisiness, during this period, CTH tends to be shallower than normal as well.

a. Vertical Structure of Temperature Anomalies over Time, relationship to ENSO, and LR', CTH', PBLH' Anomalies

To consider possible lagged ocean-atmosphere correlations, time series of temperature anomaly profiles are computed and presented in Figure 6a, smoothed using a five-month central moving mean. With the exception during several El Niño events, prior to 2013, the lower troposphere is generally cooler than normal ($\overline{T}$'= -0.27°C), followed by warmer than normal conditions after 2013 ($\overline{T'} = 0.36$°C), with especially strong positive anomalies in the years

436 preceding and in conjunction with the late 2015/early 2016 El Niño, in which the five-month
437 running-mean ONI exceeded 2°C for six months, with a peak of 2.53°C There are also some
438 instances in which anomalies first emerge above the surface or in the lower free troposphere and
439 then propagate downward to the surface; this is apparent in mid-2008 in which near-neutral to
440 weak positive T' aloft reaches the surface by mid-2009 through early 2010 in relation to that
441 year's moderate El Niño. Three pulses of positive T' aloft, in early 2013, early 2014, and then
442 early 2015 propagate downward, reaching

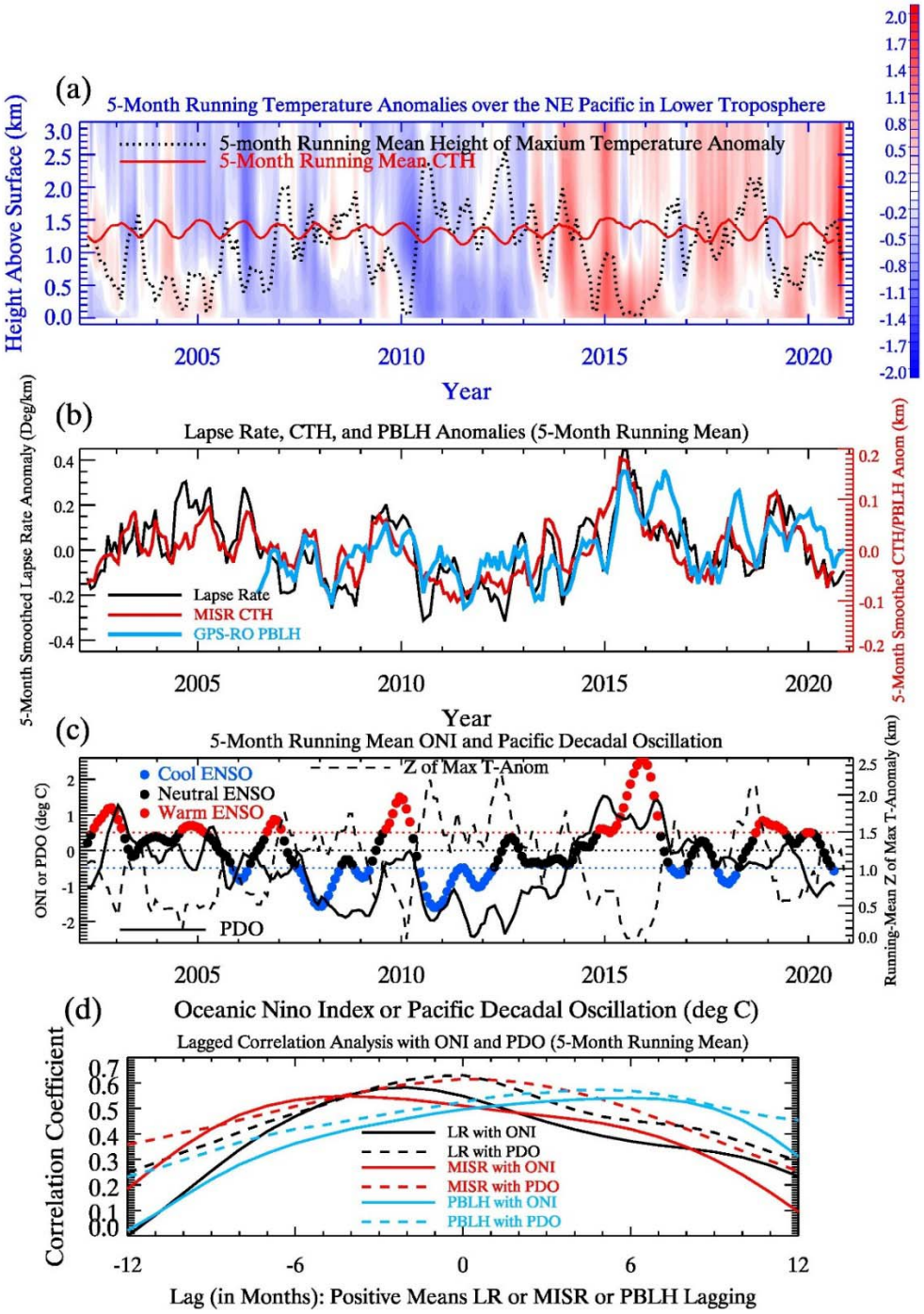

Figure 6. (a) 5-month running mean time series of temperature anomalies as a function of height, with a dashed line depicting the smoothed 5-month running mean of the height of the maximum temperature anomaly for each profile between 0-3 km. Also shown is the running mean CTH. (b) 5-month running mean time series of LR' (black curve), CTH' (red curve), and PBLH' (blue curve). (c) 5-month running mean of ONI and PDO, with 7-month running mean of the height of maximum temperature anomaly. (d) Lagged correlation analysis of LR', CTH', and PBLH' with ONI or PDO (using a 5-month running mean of each). Positive lag means LR', CTH', or PBLH' lagging.

452 the surface by mid-to-late 2015 leading up to that season's strong El Niño. We generalize these
453 lead-lag relationships momentarily.

454 Another way to see the changes in the vertical structure of T' is by examining the mean height
455 of the maximum temperature anomaly in the lowest three km of the troposphere, shown in Figure
456 6a using a 5-month running mean (dashed line). During positive ONI periods, maximum T' is
457 close to or near the surface; this is the case in early 2003 (moderate El Niño), late 2004 and again
458 in early 2005 (weak El Niño), early 2010 (moderate El Niño), late 2014 (preceding a weak El
459 Niño), and late 2015 (strong El Niño). During a few weak El Niño events (e.g. late 2006-early
460 2007, 2018-2019), max T' remains above the surface by a few hundred meters, perhaps a
461 reflection of weaker teleconnections in the NE Pacific during those events.

462 The opposite occurs during La Niña (cold ENSO) events, with maximum T' typically near or
463 above the median PBL top across the NE Pacific, with the strongest La Niñas of the record
464 during late 2007/early 2008 and late 2010/early 2011. The elevated height of maximum T' in
465 mid-2012 coincides with neutral conditions and an extended period of cold PDO values of less
466 than -2°C (Figure 6c), which start increasing by 2013. While the PDO and ENSO often are in
467 phase with each other (r=0.49 with an 5-month running mean of the 42-year datasets), they need
468 not be; between 2002-2020, mean ONI was slightly positive (0.04°C), and mean PDO modestly
469 negative (-0.50°C).While the longer-term shift towards warmer lower tropospheric temperatures
470 from 2013 onwards might be related to the shift from negative to positive PDO, in recent years
471 PDO has been generally neutral, then moving back to negative at the end of the record (Figure
472 6c).

473 Coincidentally, mid-2012 is characterized by the most suppressed LR' of the entire record;
474 CTH' was a minimum the summer prior, with a bit of recovery by mid-2012, though with
475 continued anomalously negative values.

476 The strong El Niño through early 2016 transitioned to a weak La Niña in 2016-2017 and
477 again in late 2017-2018, with corresponding increases in the altitude of maximum T'. A stronger
478 signal of the elevated height of maximum T' emerges by mid-2018; which is followed by an
479 abrupt shift to near-surface maximum T' by early 2019 following the formation of a weak El
480 Niño during late 2018 and early 2019.

481 Near-surface maximum T' generally coincides with positive CTH', PBLH', and LR' (Figure
482 6b); suggestive of a destabilization of the lower troposphere with maximum heating near the
483 surface. When the altitude above the surface of maximum T' increases, the PBL stabilizes, since
484 the anomalous warmth is near or above PBL top, representative of a stronger mean inversion,
485 and shallower low clouds and PBL heights. The temporal coherence of CTH', PBLH', and LR'
486 is generally strong, with r(PBLH', CTH')=0.63, r(LR',PBLH')=0.69, and r(LR',CTH')=0.78,
487 calculated from 5-month running mean anomalies.

488 At times, CTH', PBLH', and LR' maximize or minimize during mid-year, out-of-phase from
489 the maximum ONI signal. We quantify this with lagged correlation analysis in Figure 6d. Both
490 CTH' and LR' lead ONI maximally by four months and two months, respectively, with
491 maximum correlation values of 0.55 and 0.58, respectively. SST' also leads maximum ONI by
492 four months, with a similar r-value (not shown). In contrast, CTH' and LR' maximally correlate
493 with PDO at zero lag, with r=0.62 and 0.63, respectively.

494 In contrast, PBLH' is slightly more correlated after peak ONI; PBLH' peaks about six months
495 following the primary ONI signal, and about five months following peak PDO. We also see this

lagged behavior by direct examination of the PBLH' time series; for instance, during the summer of 2016, months after the strong El Niño peak, PBLH' remains as high as the summer prior, whereas CTH' and LR' substantially decrease. Overall, CTH' is maximally correlated with PBLH' when CTH' leads by two months (not shown).

b. Lagged Correlation Profiles

Next, we employ a rigorous filtering approach and examine lagged temperature anomaly correlation analysis with CTH', PBLH', and ONI, using the Savitzky-Golay Filter, henceforth SG-Filter. This weights the center points most, with a degree of tapering and slightly negative weighting for points further away. A boxcar filter, in contrast, weights points of n-width about a center (either temporally or spatially or both) equally. The SG-filter helps improve the signal-to-noise ratio.

In Figure 7, we present lagged correlations between either T'(z) or geopotential height anomaly (Z') with CTH', PBLH', and ONI, and show filled contours in panels (a) through (d) for correlations which exceed the 90th percentile confidence levels. These confidence levels consider the temporal autocorrelation of the variables as in Bretherton et al. (1999) by calculating the effective sample size (ESS, T^*_{XY} below) as follows:

$$T^*_{XY} = T\frac{1-r_1 r_2}{1+r_1 r_2} \quad (2)$$

where T^*_{XY} is the effective sample size for the two time series, *X(t)* and *Y(t)*, which can be CTH', PBLH', ONI, etc. In (2), r_1 and r_2 are the temporal autocorrelations at one month of *X(t)* and *Y(t)*, respectively.

In addition to the above ESS of paired variables, (2) can analogously be applied to a single variable via $T^*=T(1-r^2)/(1+r^2)$ (Bretherton et al., 1999). For an SG-Filter of width three, there are effectively 3.5 independent measurements of PBLH' per year, and 3.75 per year for CTH'. In

519 contrast, for *unsmoothed* SST', there are effectively 17 independent observations throughout the
520 period, thus approximately one each year.

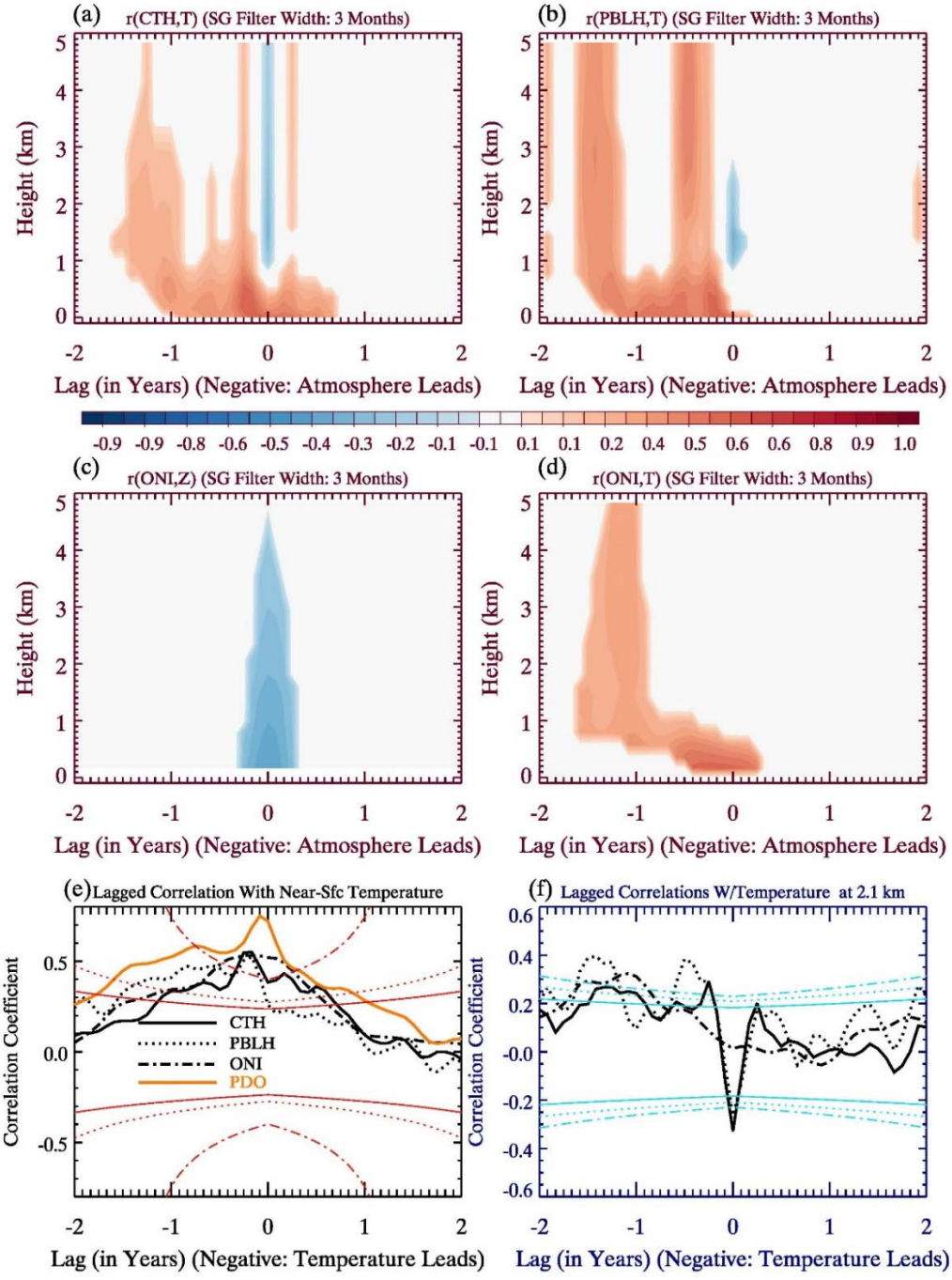

521

522 Figure 7. Paired lagged correlations with height for (a) CTH' and T'(z), (b) PBLH' and T'(z), (c)
523 ONI and geopotential height anomalies (Z'(z)), and (d) ONI and T'(z). For each, a Savitzky-Golay
524 (SG) Filter with width of three months is used, in which the weighting coefficients are 0.49 at lag
525 zero and 0.34 at lags of +/- one month. Filled contours are only shown in (a) – (d) when lagged

526 correlations exceed the 90th percent confidence levels. (e) Lagged correlations with near-surface
527 temperature. Red curves show critical correlation coefficients above/below which correlations are
528 statistically significant at the 90th confidence level. (f) Same as (e), except temperature at 2.1 km;
529 blue curves (and corresponding styles) indicate critical correlation coefficients.
530 The critical correlation coefficient above which the absolute value of the paired correlation
531 must exceed the 90% confidence level is computed as:

532 $$Corr_{crit} = \frac{1.64}{\sqrt{ESS - lag(t)}} \quad (3)$$

533 ESS in (3) comes from (2), and *lag(t)* ranges from -24 to +24 months. Statistically significant
534 correlation is more difficult to achieve with increasing lag between the two variables of interest.
535 In Figure 7a, the correlation profile is presented of CTH' and T'(z), with negative lag indicative
536 of atmospheric T' or SST' leading CTH'. At zero lag, CTH' is positively correlated with low-
537 level T' and negatively correlated with T' in the upper part of the PBL and the free troposphere;
538 suggesting an anomalously unstable profile. There is a tendency for T' at low altitudes to lead
539 CTH' (Figure 7a), with T' near the surface and aloft leading by three months and then at 12-15
540 months. CTH' also can lead low-level T'.
541 The lagged-correlation analysis between T' and PBLH' is qualitatively similar at zero lag as
542 between T' and CTH' (Figure 7b), with strongest negative correlations between 1 km and 2.5
543 km. At 2.1 km, T' is negatively correlated with PBLH' and CTH', with r around -0.3 (Figure
544 7f). In Figure 7b, there are leading atmospheric T' modes aloft, but with longer lead times with
545 PBLH' (than CTH') of about 6 months and 18 months. However, near surface T' leading
546 PBLH' by about three months is similar to the correlation of T' with CTH' (Figure 7e).
547 During El Niño, lower-than-normal geopotential heights are present in the NE Pacific at
548 zero lag, with correlations strongest near the surface, but extending upward statistically
549 significantly to nearly 5 km (Figure 7c). Given anomalous counterclockwise flow, this is
550 consistent with positive SST'/low-level T' with ONI given the anomalous southerly flow in the

551 NE Pacific. Thus, a more active storm track coincides with positive ONI (and a less active one
552 with negative ONI). Aloft, positive T', between 1 km and the free troposphere leads ONI by 12-
553 15 months, suggesting an atmospheric mode well-before ONI reaches its peak (Figure 7d; Figure
554 7f).

555 In Figure 7e, the correlation of T' near the surface with ONI is somewhat broader (than
556 between near-surface T' and CTH' or PBLH'), with a slight tendency for T' to lead slightly.
557 This is also the case for the PDO, though with higher correlation.

558 *c. Fast-Fourier Transform (FFT) Analysis of Dominant Temporal Modes*

559 To evaluate temporal modes of the variables discussed over the NE Pacific, we remove any
560 possible trend via a best linear fit approach and then apply FFT analysis by solving the
561 following, similar to Stine et al. (2009) and Kubar et al. (2012):

562 $$Y_X = \frac{2}{N}\sum_{t=0.5}^{N} \exp\left(\frac{2\pi i t}{N}\right) x(t + t_0) \quad (4)$$

563 In (4), N is the total number of months in each of the time series, which is 221 for CTH, 173 for
564 PBLH, 224 for 18-year ONI and SST time series, and 505 for the 42-year PDO and long ONI
565 time series. The factor of two incorporates positive and negative frequencies.

566 In Figure 8a, we present the fraction of total variance explained by either the 50th percentile
567 for CTH, PBLH, and SST, and the indices of ONI or PDO, as a function of period (in years); for
568 a given variable, the integrated fraction of total variance equals one. As no bandpass filtering is
569 done, the annual cycle (period of one year) stands out especially for SST (77% of the total
570 fraction of variance explained), MISR CTH (46%), and to a lesser extent GNSS-RO PBLH
571 (24%). Note the different vertical scale for SST compared to the other variables. There is also
572 higher frequency variability for PBLH and CTH; a half-year mode explains nearly 18% of the
573 total variance of PBLH, and 8% of the total variance of CTH.

574 Weak modes of multi-year periodicity of CTH and PBLH, with small peaks at ~3-years
575 explaining 3% of the total variance, coincide with a roughly 3-year ONI mode that is obtained by
576 either analyzing the 18-year time series (2002-2021) or the 42-year ONI time series from 1979-
577 2021. Spectral analysis of both ONI time series yields a 1.5-year ENSO mode; the 42-year ONI
578 contains multiple spectral peaks between 2.2-4.7 years, whereas the 18-year ONI has a broad,
579 nearly flat peak centered around 6 years. The PDO overlaps to some extent with the ONI,
580 especially at 4-5 years, though the most prominent PDO mode is an 8-10 year mode. The e-
581 folding time of the autocorrelation of ONI of 6 months is about half of the PDO (11 months).
582 Over all periods, the 42-year ONI time series has a mean periodicity of 3.9 years, the 18-year
583 ONI time series a periodicity of 2.8 years, and the PDO 5.2 years. For a thorough exploration of
584 different ENSO modes, including temporal and east versus central Pacific El Niño flavors, see
585 both Chattopadhyay et al. (2019) and Kim et al. (2012).

586 To further examine the behavior of temporal modes of CTH and PBLH across different
587 portions of the NE Pacific, we plot the fraction of variance explained by subannual modes (0.2-
588 yr to 0.8-yr), annual cycle (0.8-yr to 1.2 yr), and multi-year (1.2-yr to 7-yr) modes as a function
589 of percentile. The shallowest PBLs/clouds (5^{th} percentile) are dominated by greater subannual
590 variability than deeper PBLs/clouds, explaining over 70% and 60% of total variance for PBLH
591 and CTH, respectively. For a given percentile, the fraction of variance explained by subannual
592 variability systematically is higher by about 0.15-0.2 for PBLH versus CTH (mean difference of
593 0.2); the annual cycle is relatively more important for low cloud height variability than for
594 PBLH.

595 Finally, while multiyear variability is relevant, compared to faster modes, it only explains
596 about 6%-17% of the total variance of both PBLH and CTH. When the annual cycle is removed,

however, the interannual mode overall is approximately twice as important, with some sensitivity (especially for CTH) to the regime (percentile) (not shown).

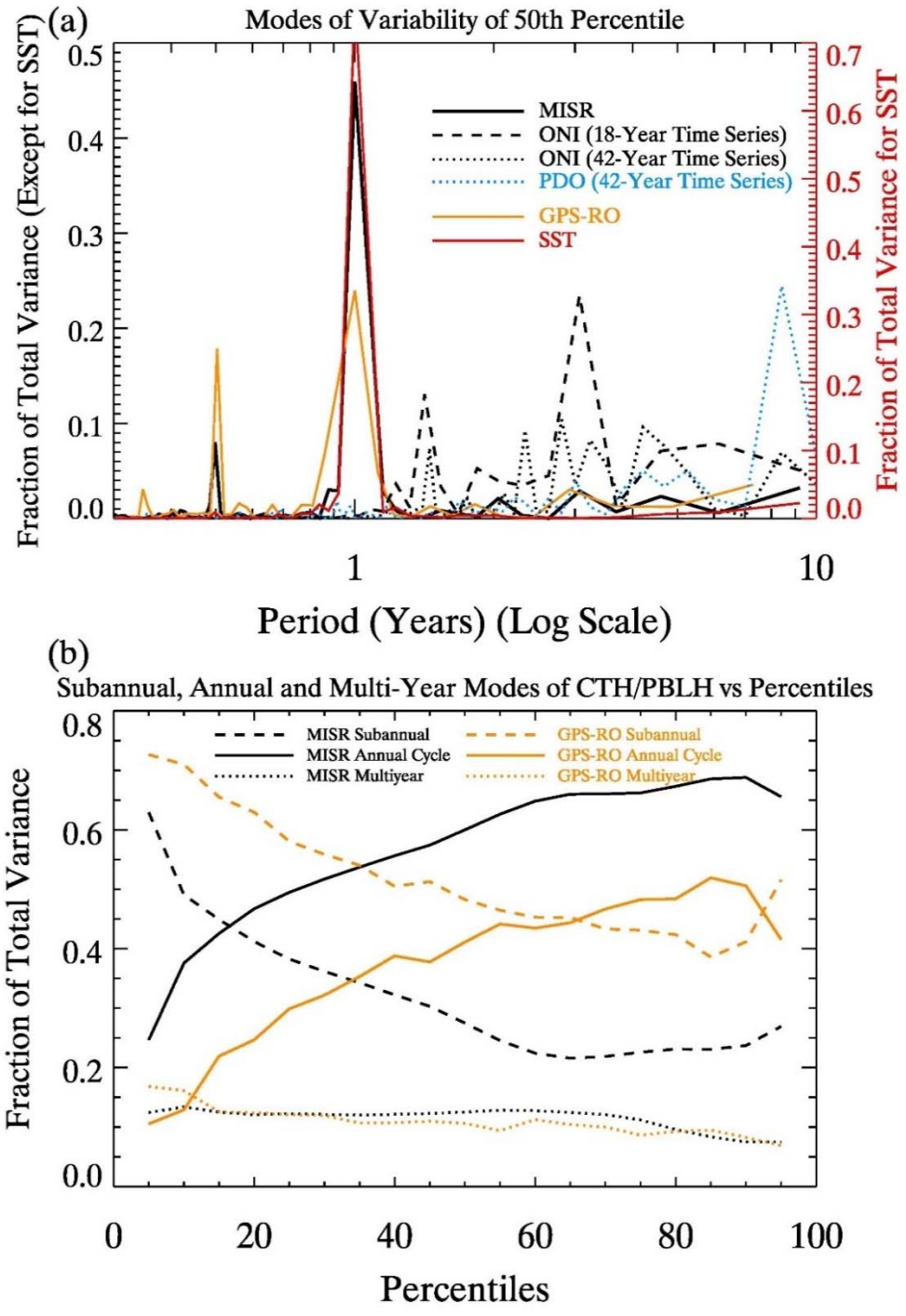

Figure 8. (a) Modes of variability in years (period) at the 50th percentile for CTH, PBLH, SST, ONI, and the PDO time series using the fast Fourier Transform (FFT) function. The ONI FFT analysis is based on both 42 years and 18 years; PDO is based on 42 years. (b) Fraction of

603 variance explained by subannual (0.2-yr to 0.8-yr), annual cycle (0.8-yr to 1.2-yr) and multi-year
604 modes (1.2-yr to 7 years) for PBLH and CTH percentiles.
605

606 **5 Discussion and Summary**

607 In this study, we have presented a spatiotemporal analysis of PBLH from GNSS-RO, CTH
608 from MISR, and temperature profile data with a focus on the SST to 700 hPa LR from ERA5
609 reanalysis data to characterize PBL and cloud height variability on seasonal to interannual time
610 scales over the Northeast Pacific. Building upon previous work, our analysis indicates that
611 PBLH and CTH are most spatiotemporally coherent when seasonal temperatures aloft (at 700
612 hPa) are greater than 4°C, helping to filter out the effects of mean-tropospheric ascent and the
613 storm track, with the most improvement during DJF and MAM. The best agreement between
614 PBLH and CTH is over stratus and stratocumulus regimes, and mean CTH is below PBLH in the
615 southwestern part of the domain where trade cumulus and shallow convective clouds dominate.

616 Both PBLH and CTH are spatially correlated with LR seasonally with r(LR,CTH)=0.88 and
617 r(LR,PBLH)=0.73 for all seasons using exponential fits. A subset of low clouds during DJF and
618 MAM have heights above the anticipated best (LR, CTH) fit, which are modulated by stronger
619 upward vertical velocity at 500 hPa (ω_{500}). Seasonal CTH monotonically increases with
620 decreasing ω_{500}, whereas PBLH is fixed at about 1.5 km for near-neutral or ascending seasonal
621 grids at 500 hPa. For all grids and all seasons, r(PBLH,CTH) = 0.62, whereas for ω_{500} > 5 mb
622 day^{-1}, r=0.74 when considering all seasons, and for seasonal T_{700}>4°C, r=0.83.

623 Consistent with good spatial coherence between PBLH and CTH over shallower PBLs, the
624 25^{th} percentile time series of CTH and PBLH agree well with each other in terms of annual cycle
625 amplitude (r=0.72). The temporal correlation gradually degrades above the 50^{th} percentiles in
626 part due to different locations of the deepest PBLs versus the deepest CTH, and annual cycle

627 amplitudes of CTH for percentiles above the 60th exceed those of PBLH annual cycle
628 amplitudes. While CTH is well correlated temporally with LR, percentiles of CTH versus LR
629 resemble an exponential increase of CTH since the standard deviation of CTH increases with
630 percentiles.

631 Hovmöller diagram analysis reveals that CTH', LR', and SST' tend to be positive during
632 periods of El Niño or warm ENSO in general, and negative during periods of La Niña or cold
633 ENSO in general. Spatiotemporal correlation between CTH' and LR' is higher than between
634 CTH' and SST', though spatiotemporal r-values increase for each pair with additional data
635 smoothing. While CTH' is weakly correlated with T700', LR' and T700' are well-correlated
636 spatiotemporally with no smoothing (r = -0.71), suggesting that troughs associated with cold
637 temperatures aloft serve to strongly enhance regional lapse rates at the monthly time scale.

638 There are instances of west-to-east propagation of positive CTH', LR', and SST' across the
639 analyzed domain, especially preceding the strong 2015-2016 El Niño event, and also of negative
640 LR' and SST' during persistent negative ONIs (2011-2013). In general, the largest anomalies
641 and temporal standard deviations of CTH', LR', and SST' tend to be observed closer to the coast
642 during either phase of ENSO than over the open ocean.

643 Interannual variability analysis of CTH', PBLH', and LR' shows temporal correlation among
644 all three variables, largely in concert with both ENSO and the PDO. Especially during the
645 strongest El Niño (2015-2016), but also some other ENSO events, CTH' and LR' tend to peak
646 the summer before the peak of ENSO during the subsequent winter, though this leading of low
647 clouds and lapse rate is not always the case; CTH' and LR' are slightly more in phase with the
648 PDO, whereas PBLH' lags both indices by a few months.

649 We also show that the height of the maximum temperature anomalies in the lower 3km of the
650 troposphere oscillates between near or above the PBL top during La Niña and near the surface
651 during El Niño, suggesting the mechanism of shoaling (deepening) of the PBL during La Niña
652 (El Niño) through the stabilizing (destabilizing) effect of the PBL and lower free troposphere.
653 Lower tropospheric temperature anomalies tend to be negative more often than not prior to 2013
654 (T'=-0.27°C), consistent with a decreasing PDO during that period, with then sustained positive
655 temperature anomalies from 2013 onward (T'=0.37°C) , and a higher mean value of the PDO.
656 There is also stronger 500 mb subsidence pre-2013 (23.5 mb day^{-1}) versus 2013 onward (19.0
657 mb day^{-1}). Our results suggest the profound influence of both the teleconnections associated
658 with tropical SST (ENSO) and the broader North Pacific (PDO) on the vertical structure of the
659 PBL in the NE Pacific.
660 While just over 14 years of PBLH observations from GNSS-RO or 18+ years of CTH
661 observations from MISR are not adequate to infer potential characteristics about longer-term
662 variability, we note that there are two enhanced periods of CTH', LR' and even ONI, suggestive
663 of the PDO possibly at play in terms of describing a nearly one-decade wavelength. While
664 higher frequency ENSO spectral modes are more prominent, a weaker, slower 8-10 year-mode
665 also exists, and furthermore central Pacific ENSO variability may be operating at a slower 7-11-
666 year spectral peak (Kim et al., 2012). That this sort of variability may be apparent in the satellite
667 record warrants not only further investigation, but strongly argues for continuity of these cloud
668 and PBL datasets into the future, and also implies the important consideration of slower time
669 scales when analyzing longer satellite records (i.e. ISCCP). Finally, these modes offer a critical
670 testbed for climate models, not just in terms their ability to simulate these climate indices with
671 fidelity, but also the response of low cloud height and PBL height variability.

6 Acknowledgements

The research described in this paper was carried out with support from National Aeronautics and Space Administration (NASA) ROSES Grant 14-GNSS14-0017 (WBX 509496.02.08.08.01) and NASA GSPRO task (WBS 281945.02.03.07.60), as well as support from the MISR Science Team. Part of this research was carried out at the Jet Propulsion Laboratory, California Institute of Technology, under a contract with the National Aeronautics and Space Administration.

Open Research

Data Availability

Analyzed data from this study are available from the JPL repository at https://genesis.jpl.nasa.gov/ftp/publication_data/Kubar_etal_JGR/. Data used to calculate MISR cloud top heights as described in the text are publicly available at https://doi.org/10.5067/Terra/MISR/MIL3MCFA_L3.001. Regional PBL heights as analyzed are available at the aforementioned repository. ERA5 SST and ω and temperature pressure-level data are available at https://doi.org/10.24381/cds.f17050d7 and https://doi.org/10.24381/cds.6860a573 and described by Hersbach et al. (2023a; 2023b). Analyses were performed and figures were generated using IDL (Interactive Data Language) software from L3Harris Geospatial software licensed for use by Jet Propulsion Laboratory. Links to ENSO and PDO data time series are described and provided in the main text.

References:

Andersen, H., Cermak, J., Zipfel., L., & Myers, T. A. (2022). Attribution of observed recent decrease in low clouds over the northeast Pacific to cloud-controlling factors. *Geophysical Research Letters, 49,* e2021GL096498. https://doi.org/10.1029/2021GL096498.

Arakawa, A., & Schubert, W. H. (1974). Interaction of a cumulus cloud ensemble with the large-scale environment, Part I. *Journal of the Atmospheric Sciences, 31*(3), 674-701, https://doi.org/10.1175/1520-0469(1974)031<0674:loacce>2.0.Co;2

Boucher, O., Randall, D., Artaxo, P., Bretherton, C., Feingold, G., Forster, P., et al. (2013). Clouds and aerosols. In T. F. Stocker, D. Qin, G. K. Plattner, M. Tignor, S. K. Allen, J. Boschung, et al. (Eds.), *Climate change 2013: The physical science basis, contribution of working group I to the fourth assessment report of the intergovernmental panel on climate change.* Cambridge University Press.

Bretherton, C. S., Widmann, C., Dymnikov, V. P., Wallace, J. M., & Blade, I. (1999). The effective number of spatial degrees of freedom of a time-varying field. *Journal of Climate, 12(7),* 1990-2009, https://doi.org/10.1175/1520-0442(1999)012<1990:Tenosd>2.0.Co;2

Bretherton, C. S., & Wyant, M. C. (1997). Moisture transport, lower-tropospheric stability, and decoupling of cloud-topped boundary layers. *Journal of the Atmospheric Sciences, 54*(1), 148-167, https://doi.org/10.1175/1520-0469(1997)054<0148:Mtltsa>2.0.Co;2

Chan, K. M., & Wood, R. (2013). The seasonal cycle of planetary boundary layer depth determined using COSMIC radio occultation data. *Journal of Geophysical Research: Atmospheres, 118*(22), 12422-12434, https://doi.org/10.1002/2013JD020147

Chattopadhyay, R., Ajit Dixit, S., and Goswami, B. N. (2019). A model rendition of ENSO diversity. *Scientific Reports, 9*(1), https://doi.org/10.1038s41598-019-50409-4

Copernicus Climate Change Service, Climate Data Store, (2023a): ERA5 monthly averaged data on single levels from 1940 to present. Copernicus Climate Change Service (C3S) Climate Data Store (CDS), DOI: 10.24381/cds.f17050d7 (Accessed on DD-MMM-YYYY).

Copernicus Climate Change Service, Climate Data Store, (2023b): ERA5 monthly averaged data on pressure levels from 1940 to present. Copernicus Climate Change Service (C3S) Climate Data Store (CDS), DOI: 10.24381/cds.6860a573 (Accessed on 05-05-2023).

Davies, R. (2018). ENSO and teleconnections observed using MISR cloud height anomalies. *Remote Sensing, 11*(32), https://doi.org/10.3390/rs11010032

De Szoeke, S. P., Verlinden, K. L., Yuter, S. E., & Mechem, D. B. (2016). The time scales of variability of marine low clouds. *Journal of Climate, 29*(18), 6463-6481, https://doi.org/10.1175/jcli-d-15-0460.1

Dey, S., Gupta, S., Chakraborty, A., & Sibanda, P. (2018). Influences of boundary layer phenomena and meteorology on ambient air quality status of an urban area in eastern India. *Atmosfera 31*(1), 69-86, https://doi.org/10.20937/ATM.2018.31.01.05

Di Girolamo, L., Menzies, A., Zhao, G., Mueller, K., Moroney, C., & Diner, D. J. (2010). Multi-angle imaging SpectroRadiomer (MISR) cloud fraction by altitude algorithm theoretical basis document. Available online: https://eospso.gsfc.nasa.gov/sites/default/files/atbd/MISR_CFBA_ATBD.pdf

Hartmann., D. L., Ockert-Bell, M. E., & Michelsen, M. L. (1992). The effect of cloud type on Earth's energy balance: Global analysis. *Journal of Climate, 5,* 1281-1304, https://doi.org/10.1175/1520-0442(1992)005<1281:teocto>2.0.co;2

Hersbach, H., Bell, B., Berrisford, P., Hirahara, S., Horányi, A., Muñoz-Sabater, J., Nicolas, J., Peubey, C., Radu, R., Schepers, D., Simmons, A., Soci, C., Abdalla, S., Abellan, X., Balsamo, G., Bechtold, P., Biavati, G., Bidlot, J., Bonavita, M., De Chiara, G., Dahlgren, P., Dee, D., Diamantakis, M., Dragani, R., Flemming, J., Forbes, R., Fuentes, M., Geer, A., Haimberger, L., Healy, S., Hogan, R. J., Holm, E., Janisková, M., Keeley, S., Laloyaux, P., Lopez, P., Lupu, C., Radnoti, G., de Rosnay, P., Rozum, I., Vamborg, F., Villaume, S., Thépaut, J.-N. (2020). The ERA5 global reanalysis. *Quarterly Journal of the Royal Meteorological Society, 146*(30), 1999-2049, https://doi.org/10.1002/qj3803

Hersbach, H., Bell, B., Berrisford, P., Biavati, G., Horányi, A., Muñoz Sabater, J., Nicolas, J., Peubey, C., Radu, R., Rozum, I., Schepers, D., Simmons, A., Soci, C., Dee, D., Thépaut, J-N. (2023a): ERA5 monthly averaged data on single levels from 1940 to present. Copernicus Climate Change Service (C3S) Climate Data Store (CDS), DOI: 10.24381/cds.f17050d7 (Accessed on 05-05-2023).

Hersbach, H., Bell, B., Berrisford, P., Biavati, G., Horányi, A., Muñoz Sabater, J., Nicolas, J., Peubey, C., Radu, R., Rozum, I., Schepers, D., Simmons, A., Soci, C., Dee, D., Thépaut, J-N. (2023b): ERA5 monthly averaged data on pressure levels from 1940 to present. Copernicus Climate Change Service (C3S) Climate Data Store (CDS), DOI: 10.24381/cds.6860a573 (Accessed on 05-05-2023).

Kalmus, P., Ao, C. O., Wang, K.-N, Manzi, M. P., & Teixeira, J. (2022). A high-resolution planetary boundary layer height seasonal climatology from GNSS radio occultations. *Remote Sensing of Environment. 276,* https://doi.org/10.1016/j.rse.2022.113037

Kanamitsu, M., Yulaeva, E., Li, H., & Hong, S.-Y. (2013). Catalina Eddy as revealed by the historical downscaling of reanalysis. *Asia-Pacific Journal of Atmospheric Sciences, 49*(4), 467-481, https://doi.org/10.1007/s13143-013-0042-x

Karlsson, J., Svensson, G., Cardoso, S., Teixeira, J., & Paradise, S. (2010). The subtropical cloud-regime transitions: boundary layer depth and cloud-top height evolution in models and observations. *Journal of Applied Meteorology and Climatology, 49*(9), 1845-1858, https://doi.org/10.1175/2010jamc2338.1

Kim, J.-S., Kim, K.-Y., & Yeh, S.-W. (2012): Statistical evidence for the natural variation of the central Pacific El Niño. *Journal of Geophysical Research, 117*(C6), https://doi.org/10.1029/2012JC008003

Klein, S., & Hartmann, D. L. (1993). The seasonal cycle of low stratiform clouds. *Journal of Climate*, *6*(8), 1587-1606, https://doi.org/10.1175/1520-0442(1993)006<1587:tscols>2.0.co;2

Klein, S. A. (1997). Synoptic variability of low-cloud properties and meteorological parameters in the subtropical trade wind boundary layer. *Journal of Climate, 10*(8), 2018-2039, https://doi.org/10.1175/1520-0442(1997)010<2018:SVOLCP>2.0.CO;2

Kubar, T. L., Hartmann, D. L., & Wood, R. (2007). Radiative and convective driving of tropical high clouds. *Journal of Climate, 20,* 5510-5526, https://doi.org/10.1175/2007JCLI1628.1

Kubar, T. L., Jiang, J. H. (2019). Net cloud thinning, low-level cloud diminishment, and Hadley circulation weakening of precipitating clouds with tropical west Pacific SST using MISR and other Satellite and Reanalysis Data. *Remote Sensing, 11*(10), https://doi.org/mdpi.com/2072-4292/11/10/1250

Kubar, T. L., Waliser, D. E., Li, J.-L., & Jiang, X. (2012). On the annual cycle, variability, and correlations of oceanic low-topped clouds with large-scale circulation using Aqua and ERA-Interim. *Journal of Climate, 25*(18), 6152-6174, https://doi.org/10.1175/jcli-d-11-00478.1

Kubar, T. L., Feiqin, X., Chi, A. O., & Loknath, A. (2020): An assessment of PBL heights and low cloud profiles in CAM5 and CAM5-CLUBB over the southeast Pacific using satellite observations. *Geophysical Research Letters, 47*(2), https://doi.org/10.1029/2019g1084498.
Medeiros, B., Hall, A., & Stevens, B. (2005): What controls the mean depth of the PBL? *Journal of Climate*, *18*(16), 3157-3172, https://doi.org/10.1175/jcli3417.1

Mantua, N. J., & Hare, S. R. (2002): The Pacific Decadal Oscillation. *Journal of Oceanography, 58*(1), 35-44, https://doi.org/10.1012/A:1015820616384

Myers, T. A., Mechoso, Cr. R., Cesana, G. V., DeFlorio, M. J., and Waliser, D. E. (2018). Cloud feedback key to marin heatwave off Baja California. *Geophysical Research Letters, 45,* 4345-4352. https://doi.org/10.1029/2018GL078242.

Randall, D. A., Coakley, J. A., Jr, Fairall, C. W., Kropfli, R. A., & Lenschow, D. H. (1984). Outlook for research on marine stratiform clouds. *Bulletin of the American Meteorological Society, 65*(12), 1290-1301. https://doi.org/10.1175/1520-0477(1984)065<1290:ofrosm>2.0.co;2

Wood, R. (2012). Stratocumulus clouds. *Mon. Weather Rev., 140*(12), 2373-2423. https://doi.org/10.1175/mwr-d-11-00121.1

Wood, R., & Bretherton, C. S. (2006). On the relationship between stratiform low cloud cover and lower-tropospheric stability. *Journal of Climate, 19*(24), 6425-6432, https://doi.org/10.1175/jcli3988.1

Wyant, M. C., Bretherton, C. S., Rand. H. A., & Stevens, D. E. (1997). Numerical simulations and a conceptual model of the stratocumulus to trade cumulus transition. *54*(1), 168-192. https://doi.org/10.1175/1520-0469(1997)054<0168:Nsaacm>2.0.Co;2

Zhang, Y., Wallace, J. M., & Battisti, D. S. (1997). ENSO-like Interdecadal Variability: 1900-93. *Journal of Climate, 10*(5), 1004-1020, https://doi.org/10.1175/1520-0442(1997)010<1004:Eliv>2.0.Co;2